Supplementary material of manuscript "Aerosol optical properties predicted from ground-based observations compared to Raman lidar retrievals during RITA-2021"

Summary of the Figures and Tables:

Figure S1: (a) An aerial view of the infrastructure setup during the RITA-2021campaign (photo by Wouter Knap, KNMI). (b) The CESAR site (marked in red) location in the Netherlands. 3

Figure S2: The frequency of the hourly average wind direction at CESAR in RITA campaign from May 7th 2021 to October 20th 2021. 3

Figure S3: Time series of (a) aerosol chemical composition mass concentration and (b) the corresponding mass fraction (c) tempeture and relative humidity (d) wind speed and wind direction from May to November in 2021. The two intensive RITA-2021 campaigns are marked with a pink background. 4

Figure S4: Example of the joined particle size distribution. (a) The volume size distribution (VSD) (dv/dlog(dp) cm^{-3}) of raw SMPS data (green dots). The VSD of APS data (blue dots). The selected APS data for fitting (yellow stars). The final joined VSD with dash line. (b) The PSD (particle number size distribution) (dn/dlogdp cm^{-3}) of SMPS (green dots), and the PSD of APS (blue dots), as well as the joined PSD (dash line). 5

Figure S5: Time series of the meteorological profiles from the ECMWF model, including the relative humidity (top graph) and Temperature (K, bottom graph) at CESAR from May to November in 2021. 6

Figure S6: The relative humidity profiles of the radiosonde (in green), and the radiometer (in blue), and ECMWF (in sky-blue) the tempeture profiles of radiosonde (in red), radiometer (in pink), and ECMWF (in orange) measured at times corresponding to Radiosonde balloon measurements during the RITA-2021 campaign. 7

Figure S7: Corresponding to Figure 3 and Figure 4 for the scattering coefficient and backscatter coefficient from the nephelometer measurements and from the calculations by assuming all sea salt in coarse mode. 8

Figure S8: Corresponding to Figure 3 and Figure 4 for the scattering coefficient and backscattering coefficient from the nephelometer measurements and from the calculations by assuming all mineral dust in coarse mode. 9

Figure S9: The CAELI Raman lidar measurements during 20:00 to 20:53 at UTC time on 2021-May-19. 10

Figure S10: Mass fractions of the chemical composition during 20:00 to 21:00 at UTC time on 2021-May-19. 10

Figure S11: The back trajectory of the air mass during 20:00 to 21:00 at UTC time on 2021-May-19. 10

Figure S12: The CAELI Raman lidar measurements during 19:59 to 21:59 at UTC time on 2021-Sep-09. 11

Figure S13: Mass fractions of the chemical composition during 21:10 to 21:40 at UTC time on 2021-Sep-09. 11

Figure S14: The back trajectory of the air mass during 21:00 to 22:00 at UTC time on 2021-Sep-09. 11

Figure S15: The CAELI Raman lidar measurements during 20:00 to 21:12 at UTC time on 2021-May-21. 12

Figure S16: Mass fractions of the chemical composition during 20:10 to 20:50 at UTC time on 2021-May-21. 12

Figure S17: The back trajectory of the air mass during 20:00 to 21:00 at UTC time on 2021-May-21. 12

Figure S18: The CAELI Raman lidar measurements during 20:00 to 22:00 at UTC time on 2021-July-29. 13

Figure S19: Mass fractions of the chemical composition during 20:00 to 21:00 at UTC time on 2021-July-29. 13

Figure S20: The back trajectory of the air mass during 20:00 to 21:00 at UTC time on 2021-July-29. 13

Figure S21: Profiles from 20:06 to 20:31 at UTC time on 2021-05-11. 14
Figure S22: Profiles from 20:06 to 21:12 at UTC time on 2021-05-12. 14
Figure S23: Profiles from 20:12 to 21:30 at UTC time on 2021-05-12. 15
Figure S24: Profiles from 19:17 to 19:32 at UTC time on 2021-05-19. 15
Figure S25: Profiles from 19:00 to 19:56 at UTC time on 2021-06-24. 16
Figure S26: Profiles from 20:25 to 21:25 at UTC time on 2021-07-08. 16
Figure S27: Profiles from 21:15 to 22:02 at UTC time on 2021-07-12. 17
Figure S28: Profiles from 20:10 to 21:12 at UTC time on 2021-07-19. 17
Figure S29: Profiles from 21:12 to 22:00 at UTC time on 2021-07-19. 18
Figure S30: Profiles from 21:02 to 22:05 at UTC time on 2021-07-29. 18
Figure S31: Profiles from 20:00 to 20:34 at UTC time on 2021-09-16. 19
Figure S32: Profiles from 17:00 to 17:56 at UTC time on 2021-09-17. 19
Figure S33: Profiles from 18:00 to 19:00 at UTC time on 2021-09-17. 20
Figure S34: Profiles from 19:00 to 20:02 at UTC time on 2021-09-17. 20
Figure S35: Profiles from 20:02 to 20:59 at UTC time on 2021-09-17. 21
Figure S36: Profiles from 18:24 to 19:27 at UTC time on 2021-09-18. 21
Figure S37: Profiles from 19:27 to 20:28 at UTC time on 2021-09-18. 22
Figure S38: Profiles from 17:23 to 18:26 at UTC time on 2021-09-20. 22
Figure S39: Profiles from 20:50 to 21:53 at UTC time on 2021-09-20. 23
Figure S40: Profiles from 18:28 to 19:15 at UTC time on 2021-09-26. 23
Figure S41: Profiles from 20:00 to 21:02 at UTC time on 2021-09-26. 24
Figure S42: Profiles from 18:08 to 19:10 at UTC time on 2021-10-04. 24

Table S1 Model data availability at the Raman lidar measurements dates for all the instruments. 25
Table S2 Lognormal fit parameters for the daily averaged APS volume size distribution from the Trolix-2019 campaign. 26
Table S3 The Refractive index, density and kappa values of the chemical composition. The values follow [a] Zou et al.(2019), [b] Düsing et al. (2021), [c] Di Biagio et al. (2019), [d] Bi et al.(2018), Di Biagio et al.(2019), Zieger et al.(2017). 26

S1 Measurements

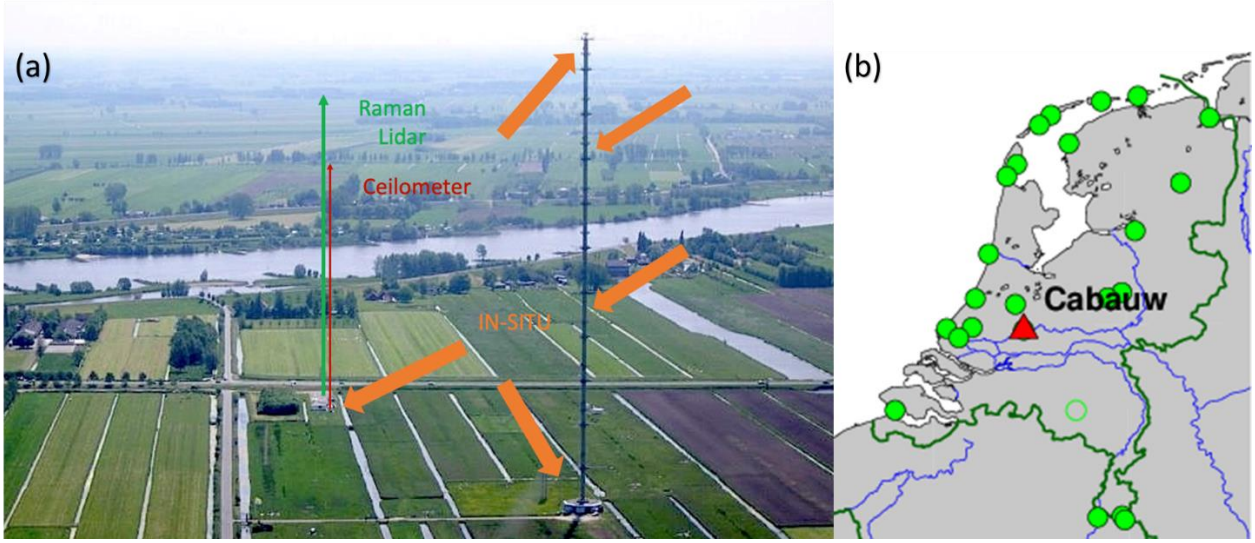

Figure S1: (a) An aerial view of the infrastructure setup during the RITA-2021campaign (photo by Wouter Knap, KNMI). (b) The CESAR site (marked in red) location in the Netherlands[1].

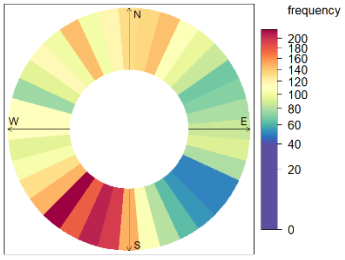

Figure S2: The frequency of the hourly average wind direction at CESAR in RITA campaign from May 7th 2021 to October 20th 2021.

[1] http://gnss1.tudelft.nl/dpga/station/Cabauw.html

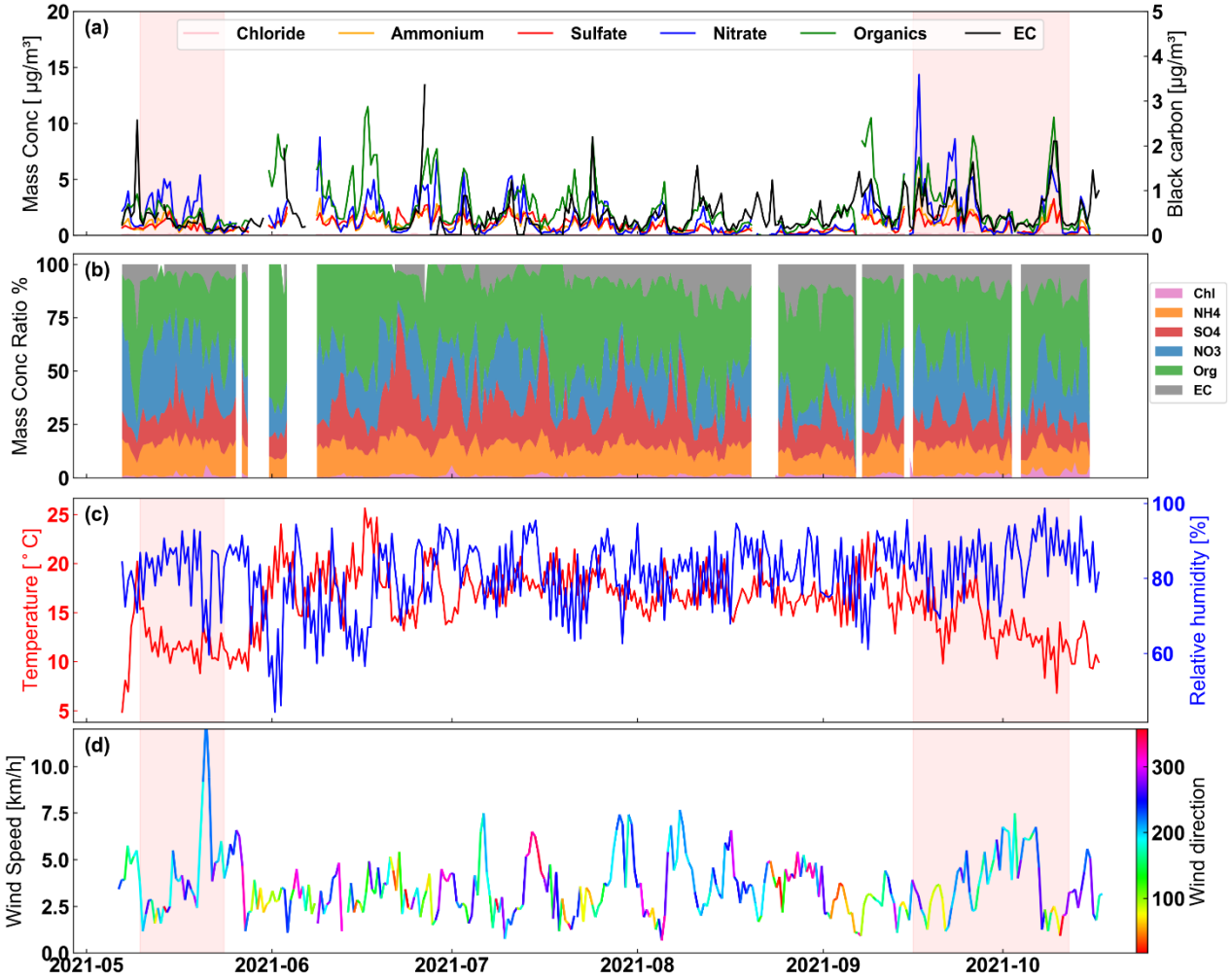

Figure S3: Time series of (a) aerosol chemical composition mass concentration and (b) the corresponding mass fraction (c) tempeture and relative humidity (d) wind speed and wind direction from May to November in 2021. The two intensive RITA-2021 campaigns are marked with a pink background.

S2 Merged particle size distribution

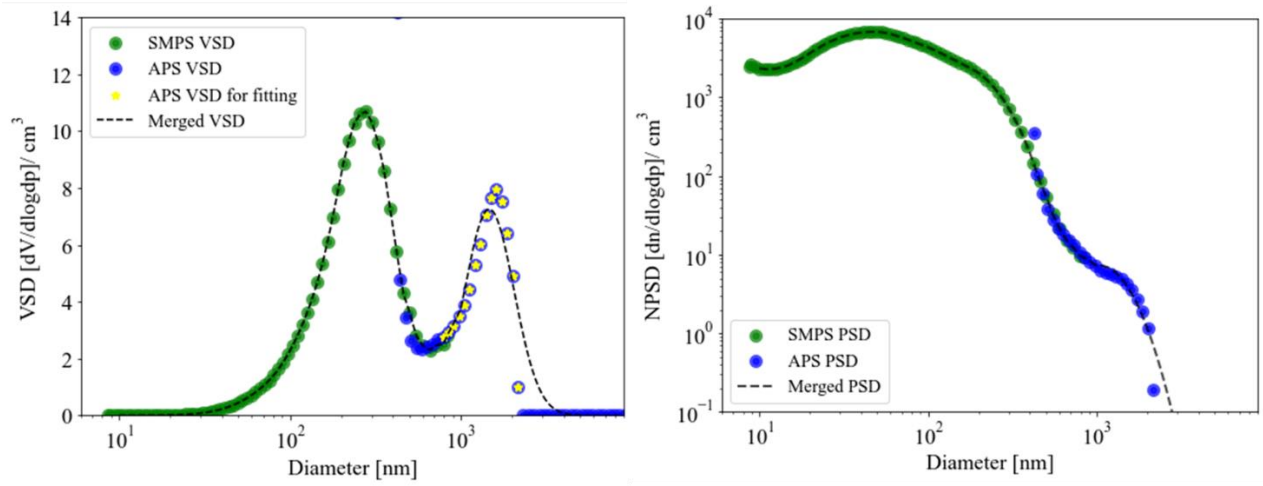

Figure S4: Example of the joined particle size distribution. (a) The volume size distribution (VSD) (dv/dlog(dp) cm^{-3}) of raw SMPS data (green dots). The VSD of APS data (blue dots). The selected APS data for fitting (yellow stars). The final joined VSD with dash line. (b) The PSD (particle number size distribution) (dn/dlogdp cm^{-3}) of SMPS (green dots), and the PSD of APS (blue dots), as well as the joined PSD (dash line).

Figure S4 shows an example of the merged particle size distribution by the SMPS and APS. The APS aerodynamic diameters were converted to volume equivalent diameters by dividing by the square root of particle effective density. The effective density was derived by an iterative approach. The volume size distribution for coarse particles (greater than 2.5 micrometres aerodynamic diameter) is converted to a mass size distribution assuming various effective densities spanning from 1.0 to 2.0 (g·cm^{-3}), with steps of 0.1. Each obtained mass distribution is then integrated to compute the total mass concentration of coarse particles. The calculated coarse mass concentrations for each assumed density are then compared to the measured coarse mode mass concentrations, determined as the difference between PM_{10} and $PM_{2.5}$ mass concentrations from gravimetric analysis. The effective density for each case is the density for which the calculated and measured coarse mode mass concentrations agree best. The average effective density is 1.6 g·cm^{-3}. For missing or unrealistic APS data, showing a sudden drop to 0 (see figure S4 a) or negative values or unrealistically high values, it was assumed that the coarse mode volume size distribution follows a lognormal distribution. The mean and standard deviation of the coarse mode was then fixed based on the coarse mode distributions that were measured during earlier Trolix campaigns in 2019. Then the lognormal distribution fitting and interpolation were performed on the obtained particle size distribution data (as shown in Figure S4). An average $\mu = 7.70$ and $\sigma = 0.46$ (shown in section S7 in TableS2) were used in the correction for the wrong APS data with fitting equation as below:

$$f(x) = \frac{1}{x\sigma\sqrt{2\pi}} \exp\left(-\frac{(lnx-\mu)^2}{2\sigma^2}\right),$$

where the x is the diameter (nm), the yellow point in FigureS3 in this case. The μ is the mean of samples in distribution, and σ is the standard deviation.

S3 Meteorological profiles

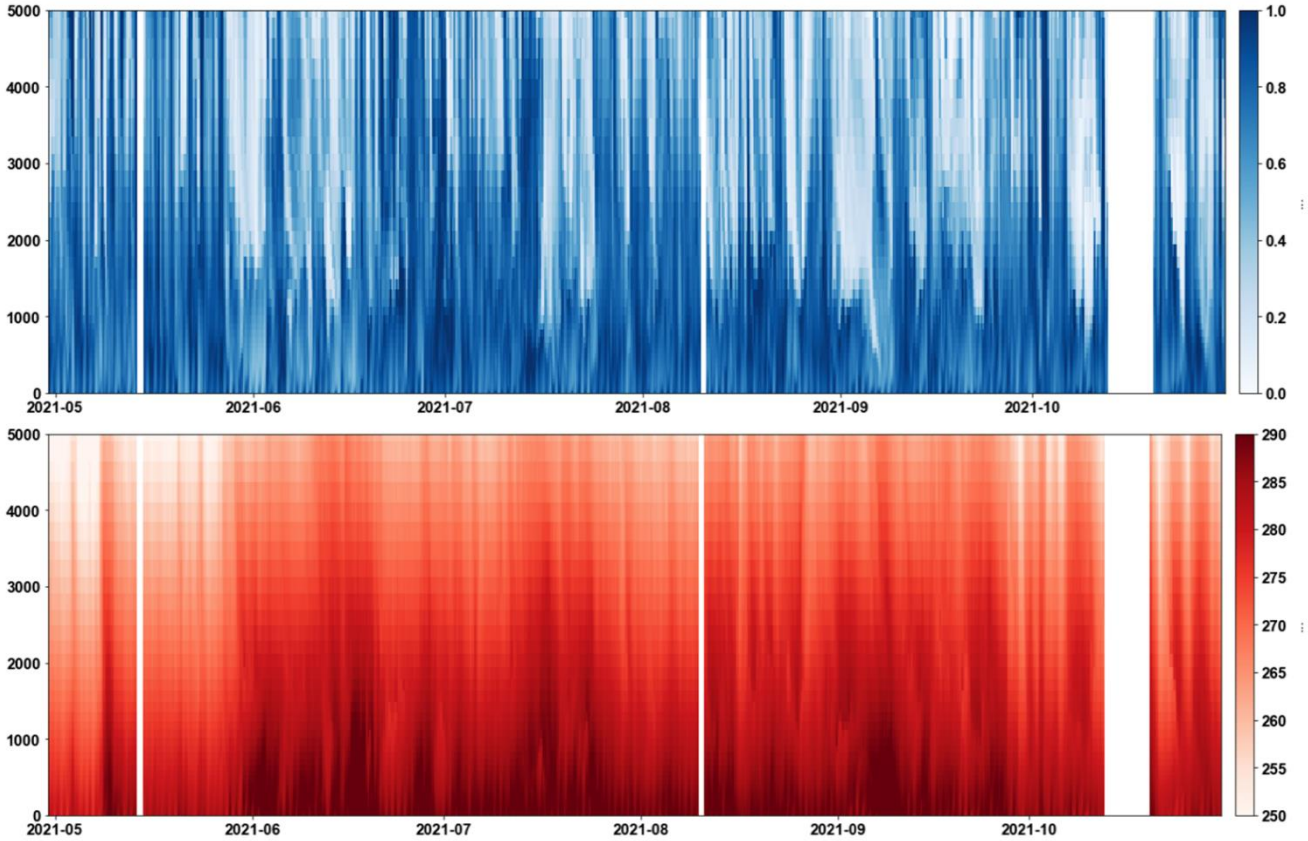

Figure S5: Time series of the meteorological profiles from the ECMWF model, including the relative humidity (top graph) and Temperature (K, bottom graph) at CESAR from May to November in 2021.

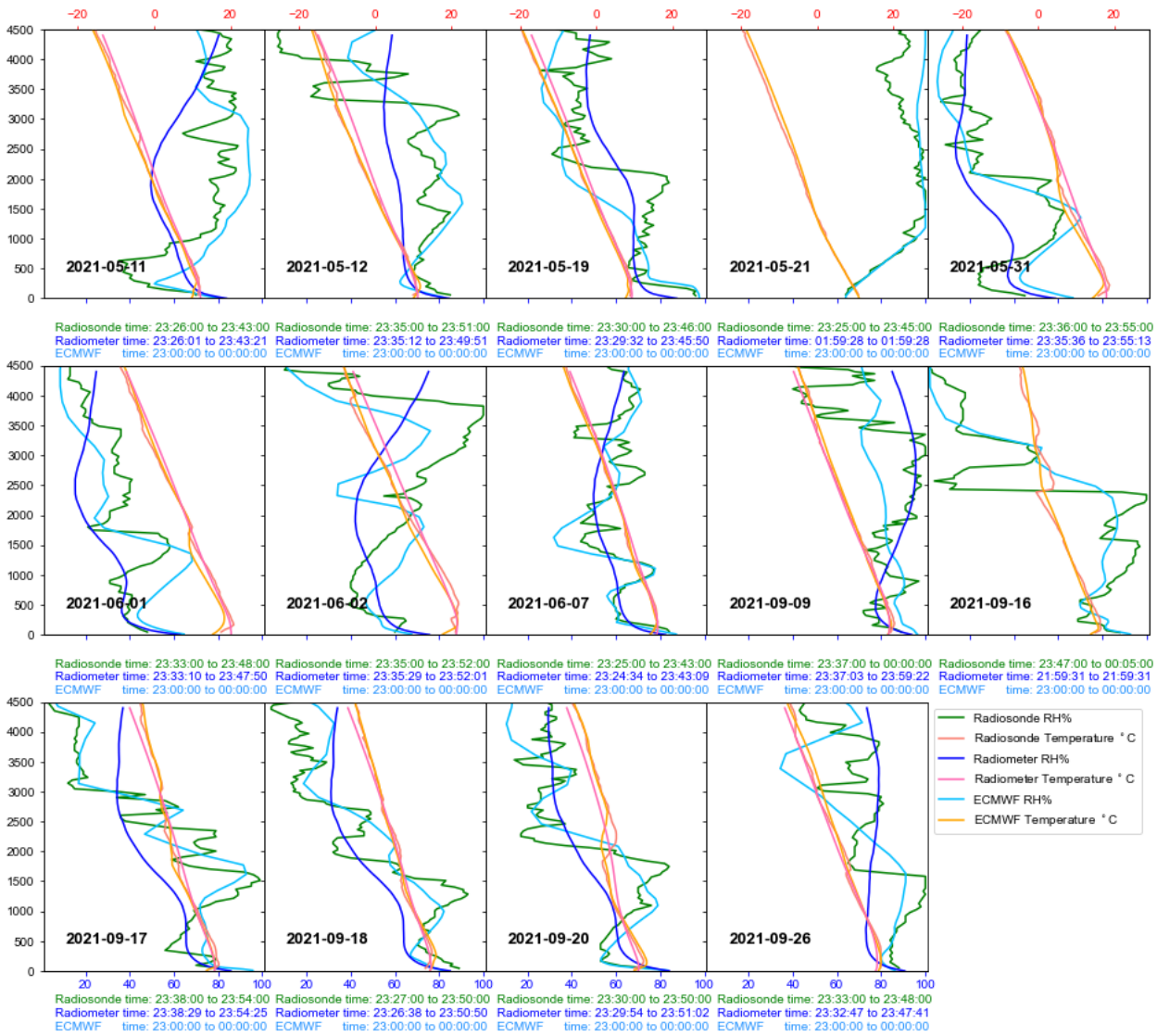

Figure S6: The relative humidity profiles of the radiosonde (in green), and the radiometer (in blue), and ECMWF (in sky-blue) the tempeture profiles of radiosonde (in red), radiometer (in pink), and ECMWF (in orange) measured at times corresponding to Radiosonde balloon measurements during the RITA-2021 campaign.

S4 Optical properties compared by calculation and Nephelometer

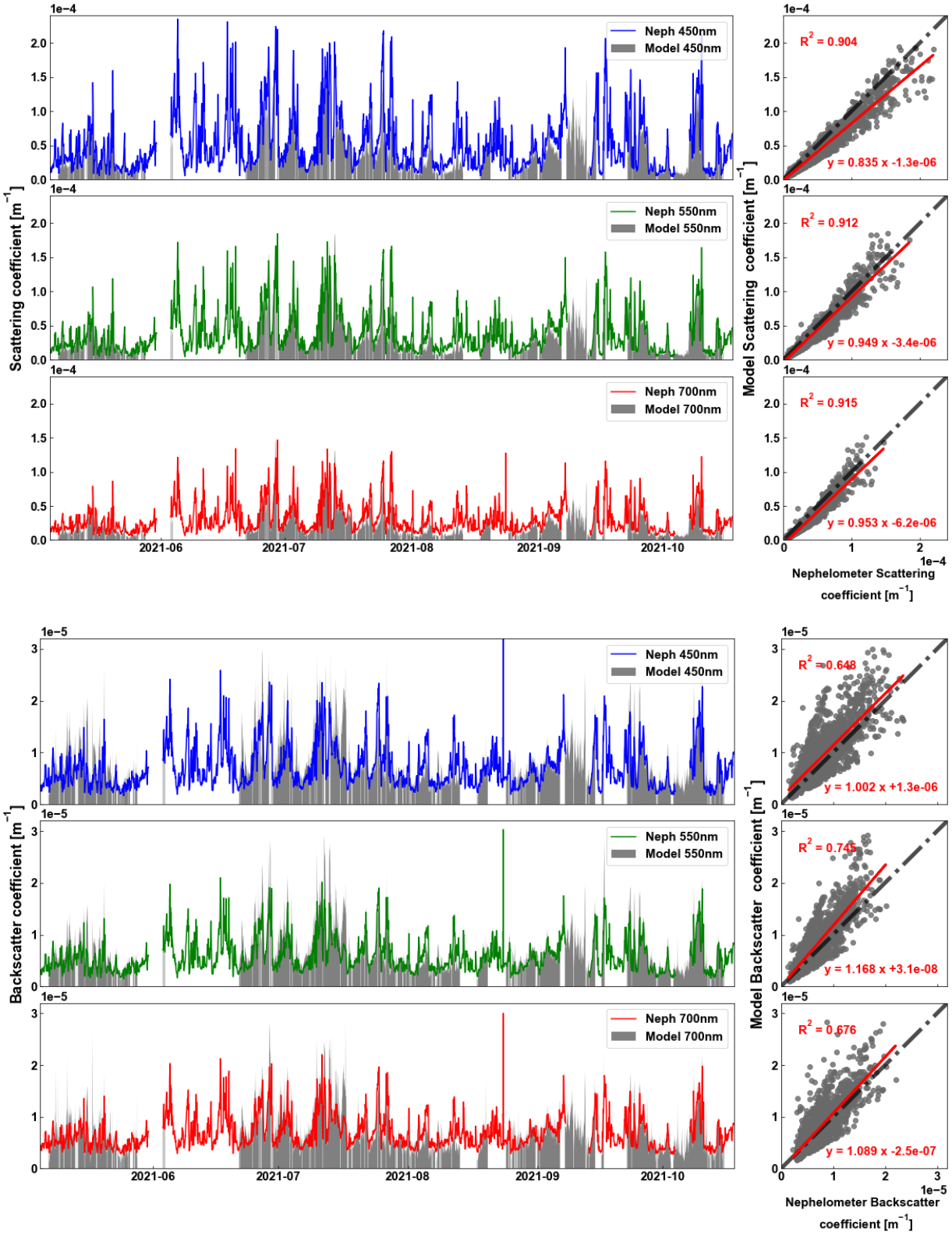

Figure S7: Corresponding to Figure 3 and Figure 4 for the scattering coefficient and backscatter coefficient from the nephelometer measurements and from the calculations by assuming all sea salt in coarse mode.

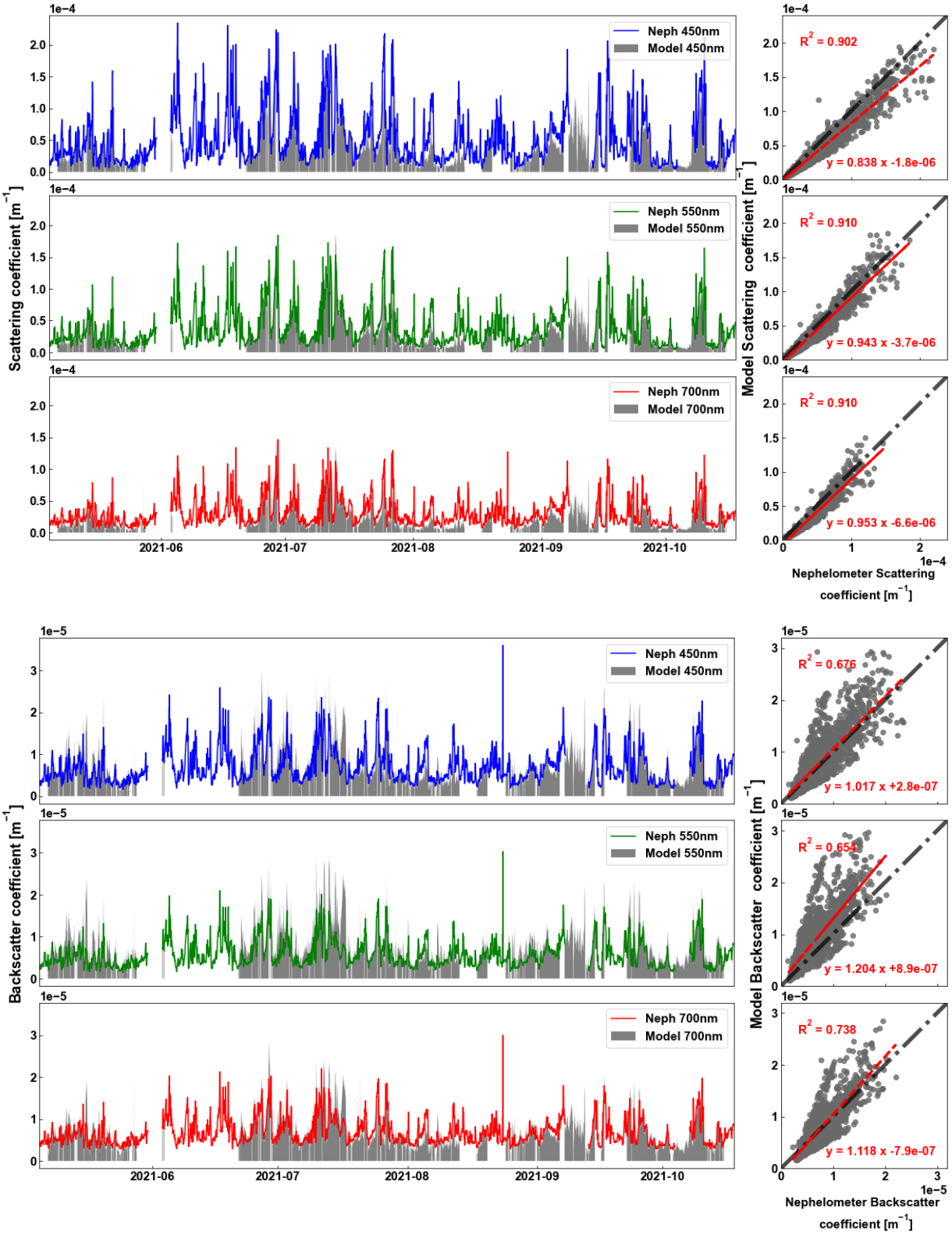

Figure S8: Corresponding to Figure 3 and Figure 4 for the scattering coefficient and backscattering coefficient from the nephelometer measurements and from the calculations by assuming all mineral dust in coarse mode.

S5 Additional information for section 3.2: Compression between the modelling and Raman lidar

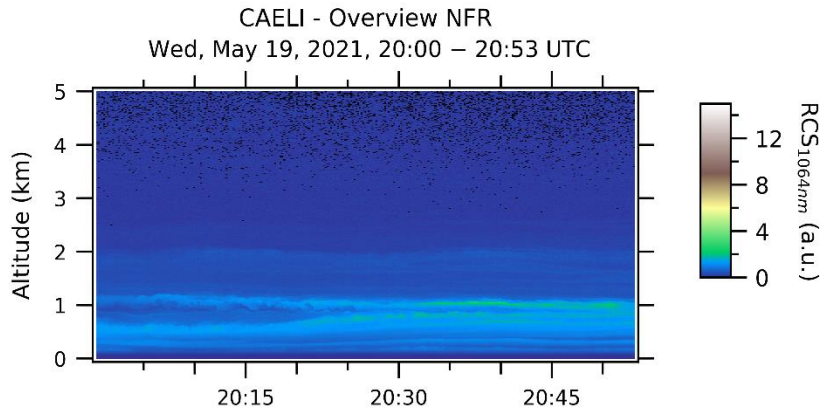

Figure S9: The CAELI Raman lidar measurements during 20:00 to 20:53 at UTC time on 2021-May-19.

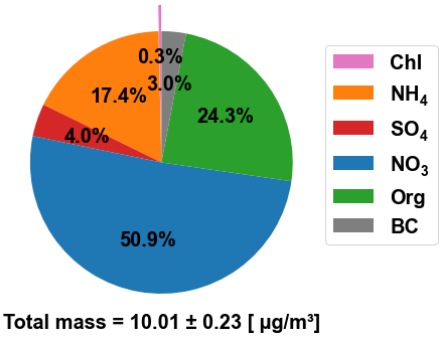

Figure S10: Mass fractions of the chemical composition during 20:00 to 21:00 at UTC time on 2021-May-19.

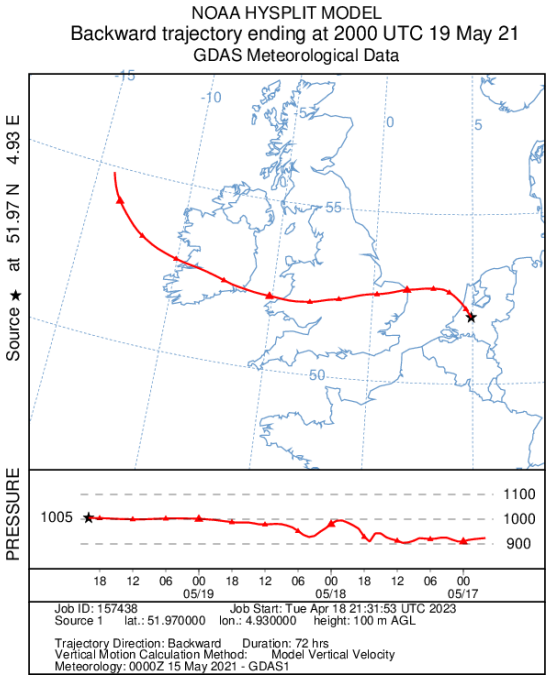

Figure S11: The back trajectory of the air mass during 20:00 to 21:00 at UTC time on 2021-May-19.

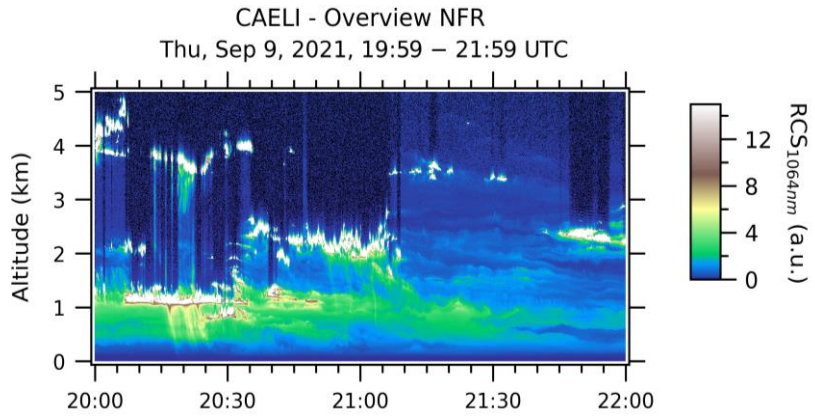

Figure S12: The CAELI Raman lidar measurements during 19:59 to 21:59 at UTC time on 2021-Sep-09.

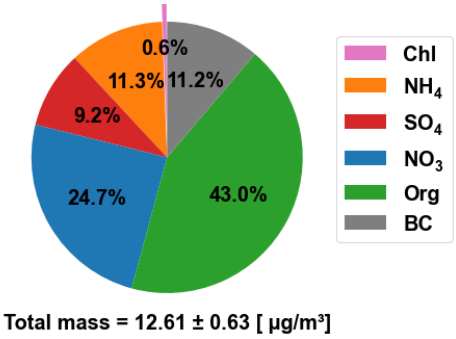

Figure S13: Mass fractions of the chemical composition during 21:10 to 21:40 at UTC time on 2021-Sep-09.

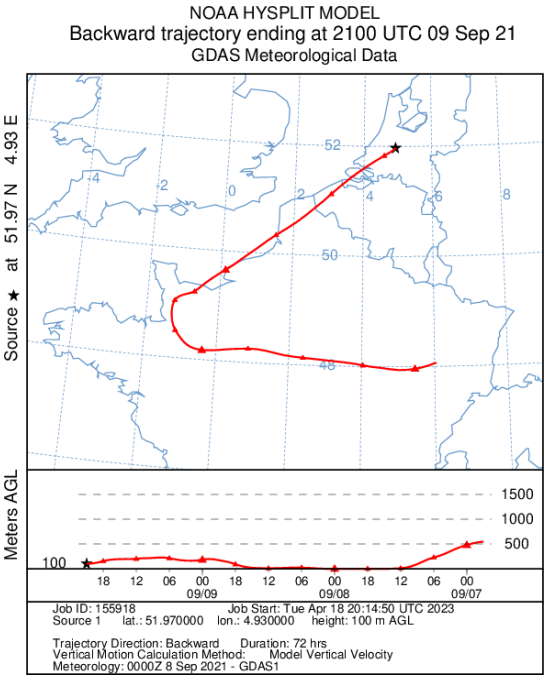

Figure S14: The back trajectory of the air mass during 21:00 to 22:00 at UTC time on 2021-Sep-09.

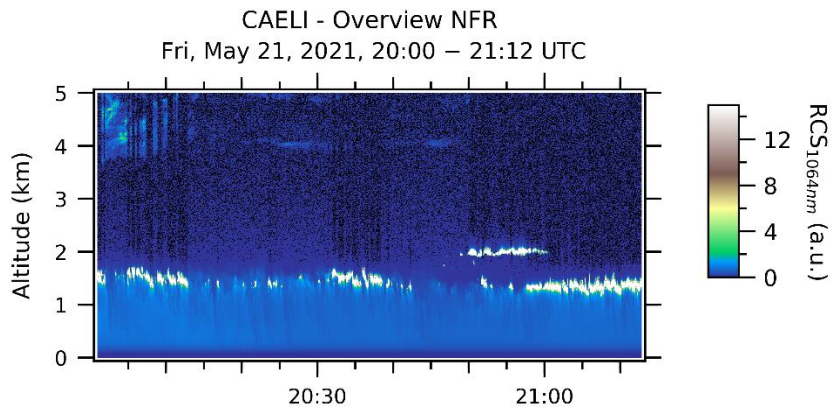

Figure S15: The CAELI Raman lidar measurements during 20:00 to 21:12 at UTC time on 2021-May-21.

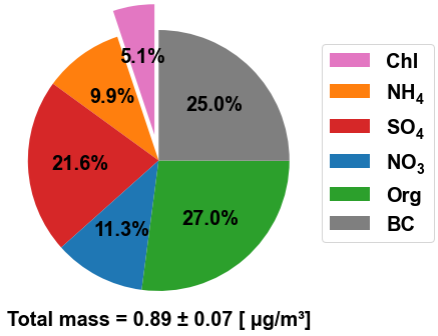

Figure S16: Mass fractions of the chemical composition during 20:10 to 20:50 at UTC time on 2021-May-21.

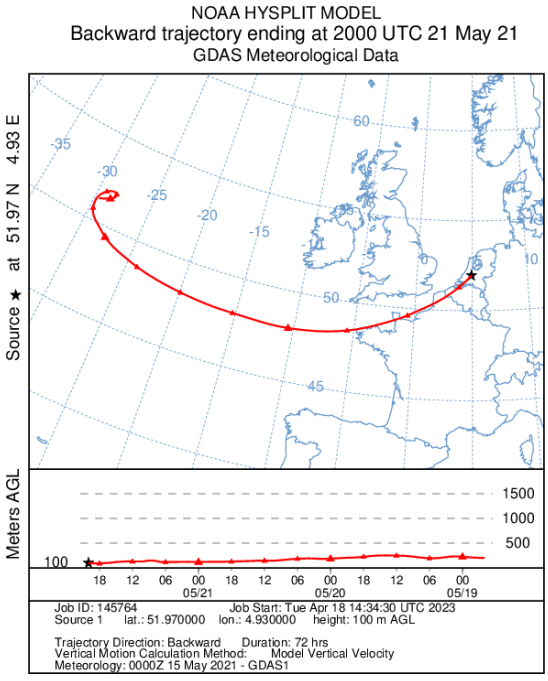

Figure S17: The back trajectory of the air mass during 20:00 to 21:00 at UTC time on 2021-May-21.

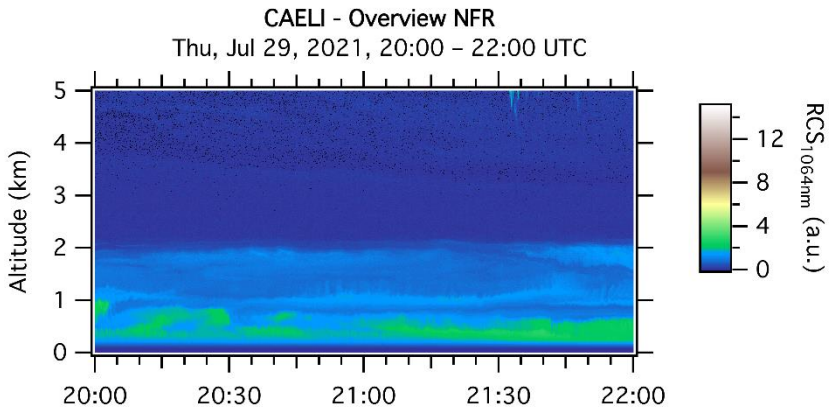

Figure S18: The CAELI Raman lidar measurements during 20:00 to 22:00 at UTC time on 2021-July-29.

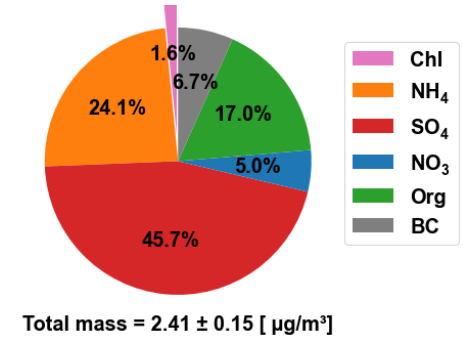

Figure S19: Mass fractions of the chemical composition during 20:00 to 21:00 at UTC time on 2021-July-29.

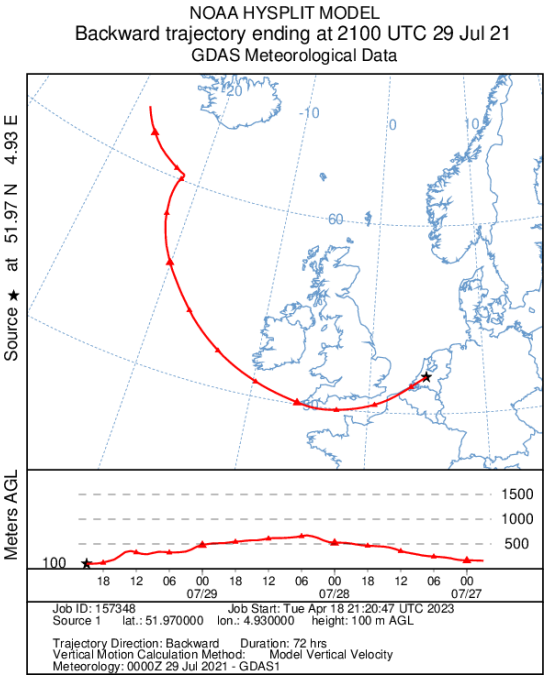

Figure S20: The back trajectory of the air mass during 20:00 to 21:00 at UTC time on 2021-July-29.

S6 Additional profiles for compression between the modelling and Raman lidar

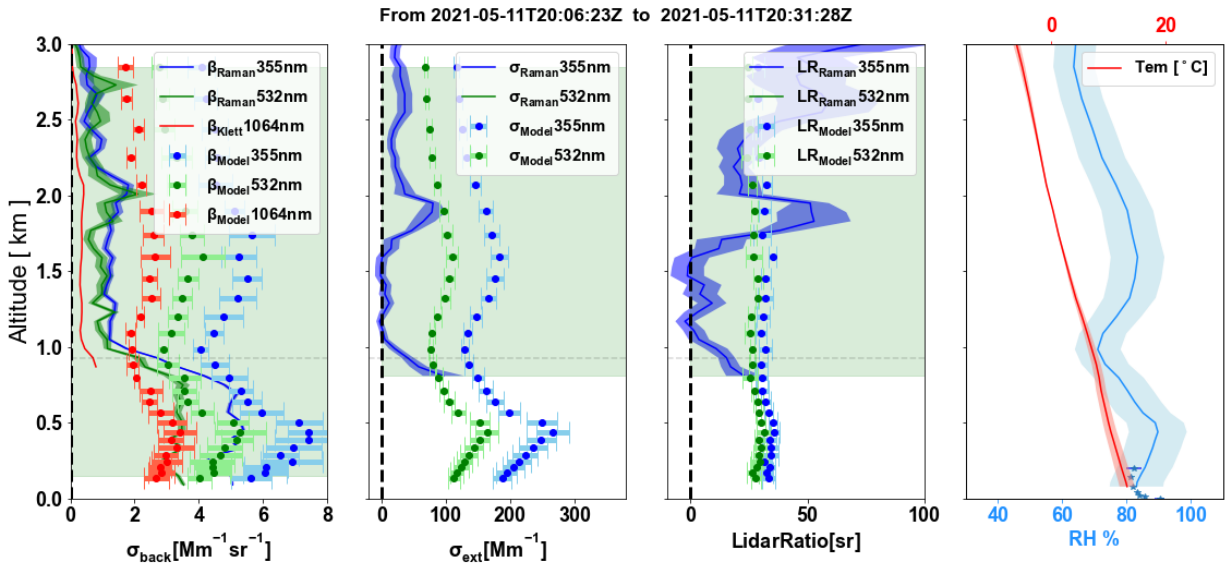

Figure S21: Profiles from 20:06 to 20:31 at UTC time on 2021-05-11.

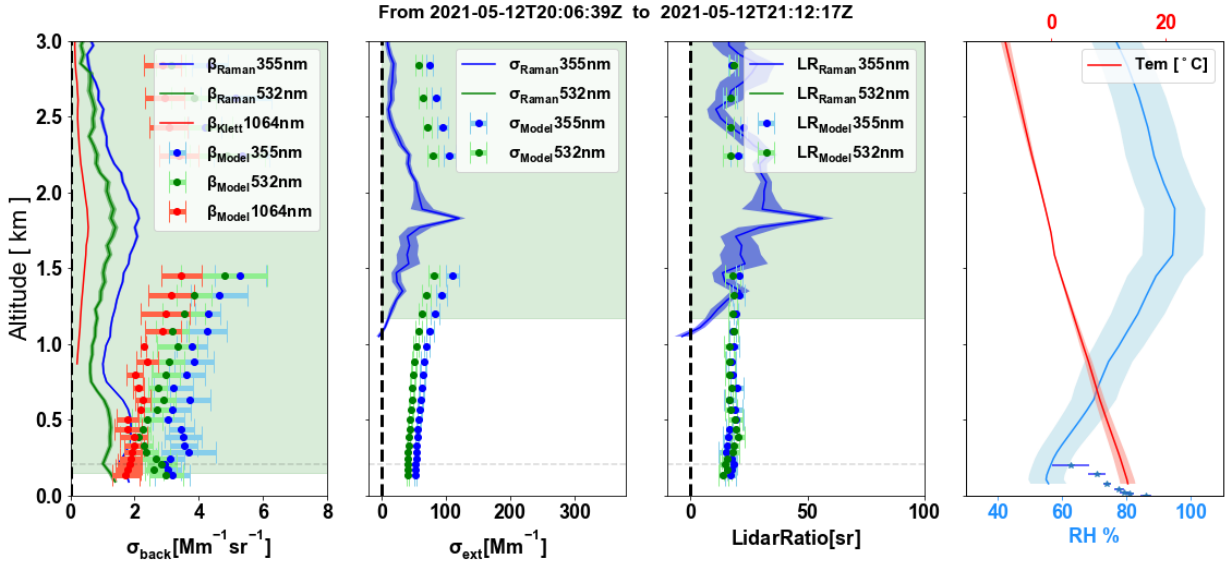

Figure S22: Profiles from 20:06 to 21:12 at UTC time on 2021-05-12.

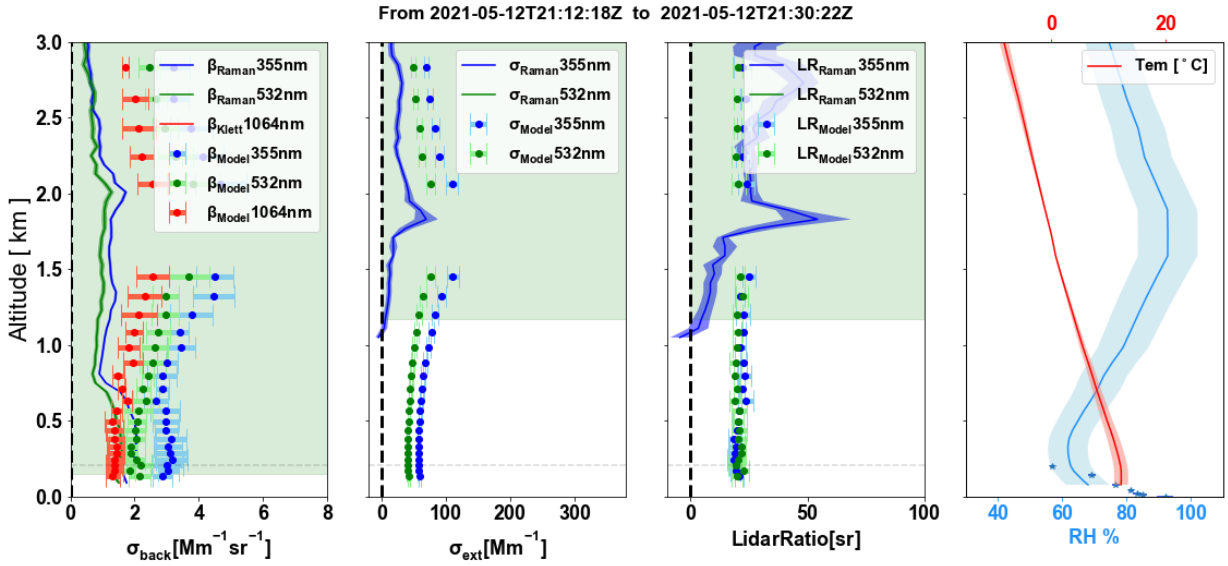

Figure S23: Profiles from 20:12 to 21:30 at UTC time on 2021-05-12.

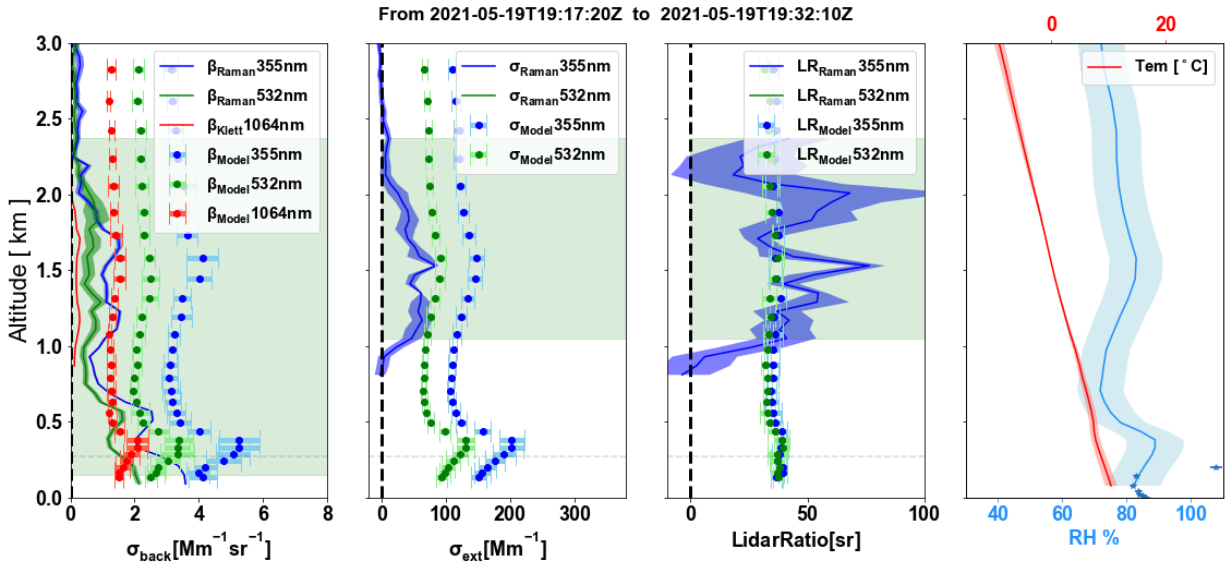

Figure S24: Profiles from 19:17 to 19:32 at UTC time on 2021-05-19.

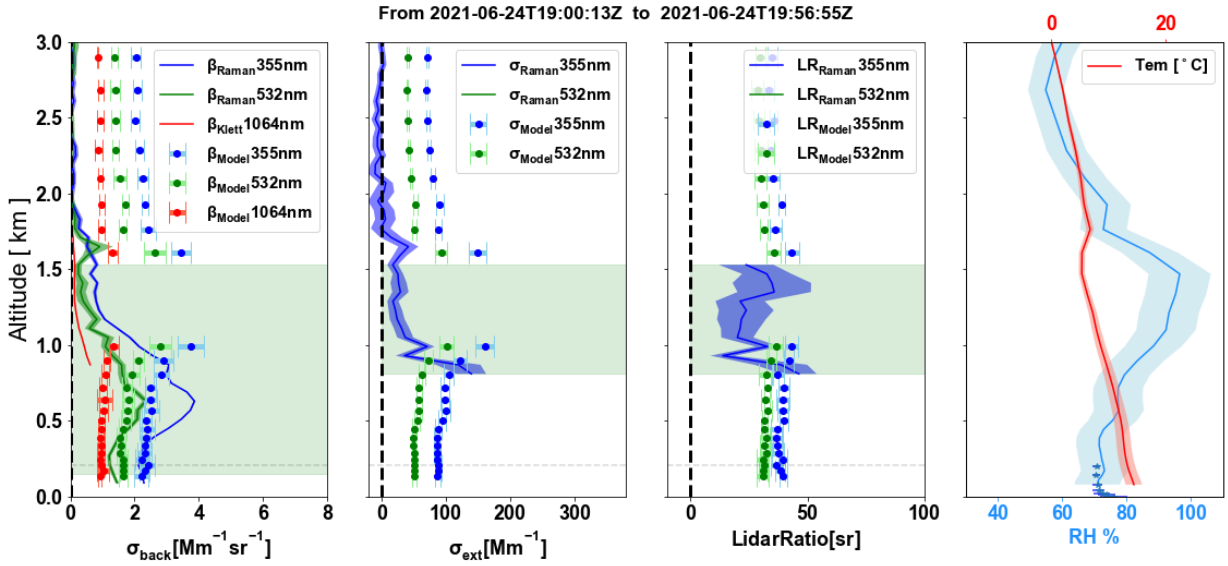

Figure S25: Profiles from 19:00 to 19:56 at UTC time on 2021-06-24.

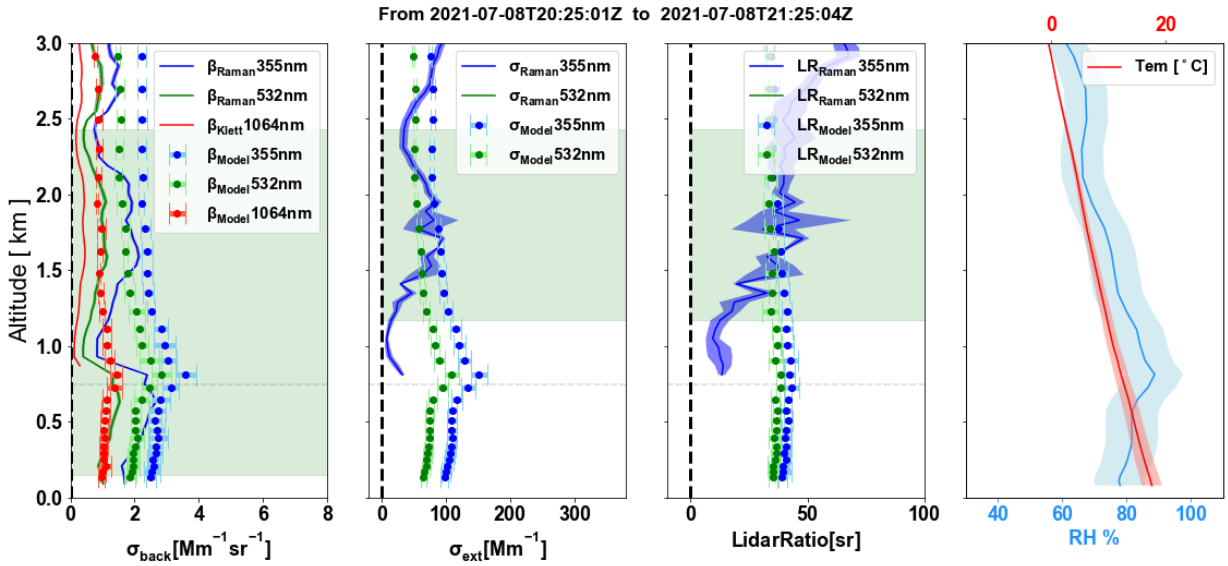

Figure S26: Profiles from 20:25 to 21:25 at UTC time on 2021-07-08.

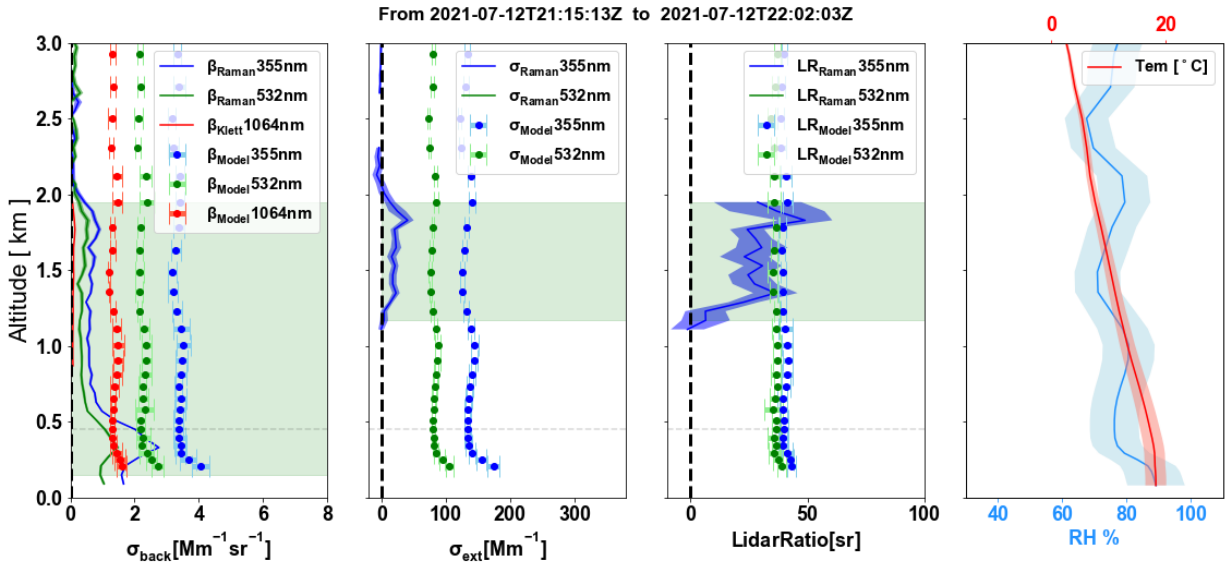

Figure S27: Profiles from 21:15 to 22:02 at UTC time on 2021-07-12.

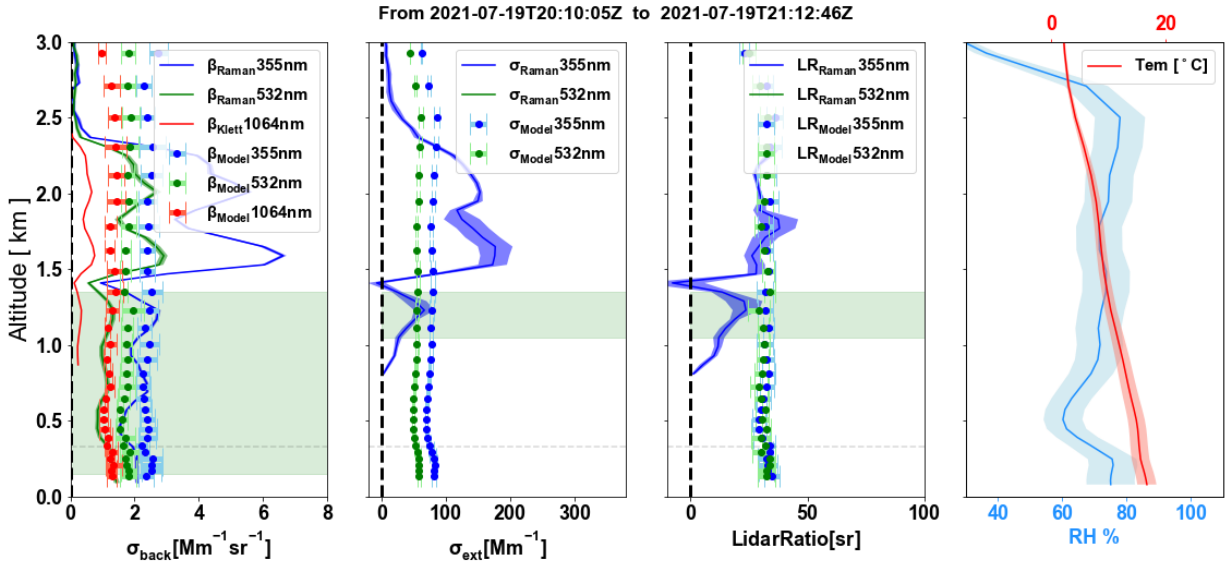

Figure S28: Profiles from 20:10 to 21:12 at UTC time on 2021-07-19.

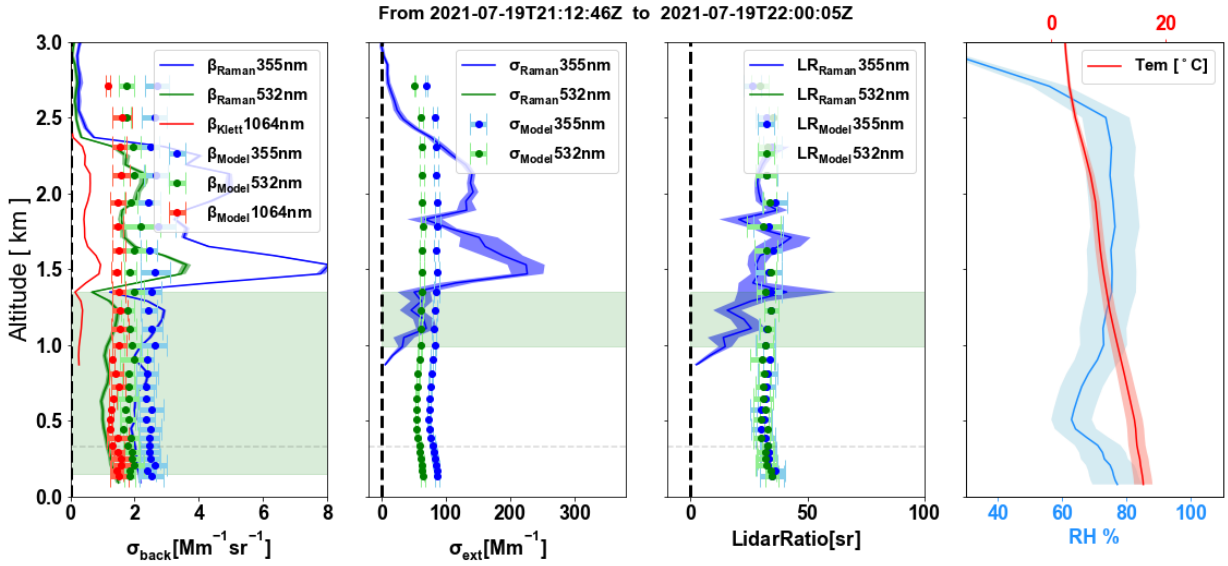

Figure S29: Profiles from 21:12 to 22:00 at UTC time on 2021-07-19.

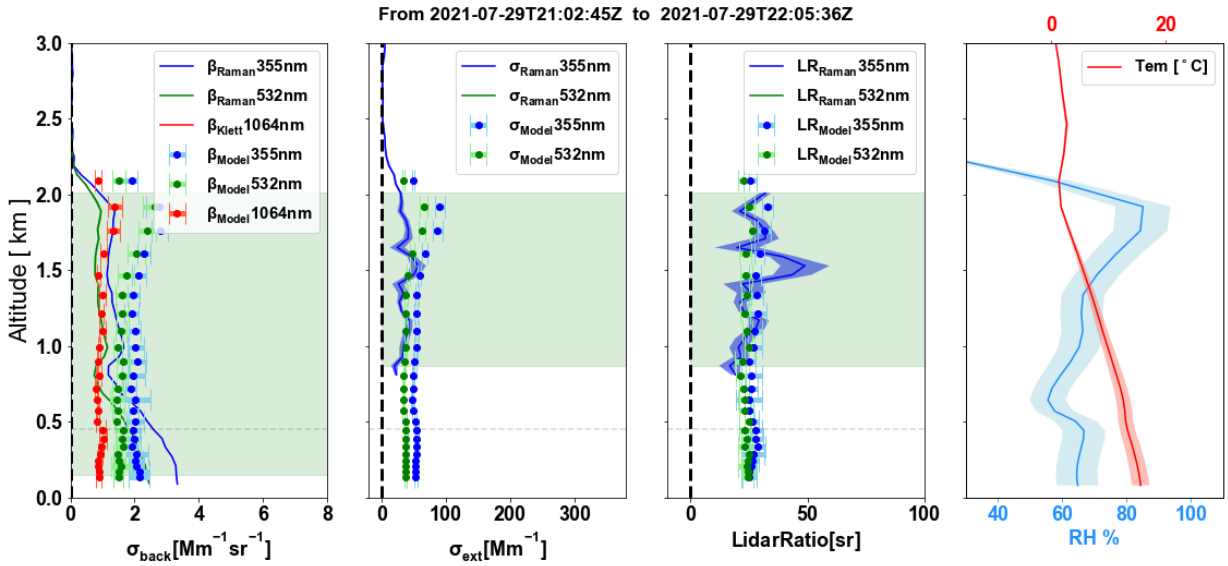

Figure S30: Profiles from 21:02 to 22:05 at UTC time on 2021-07-29.

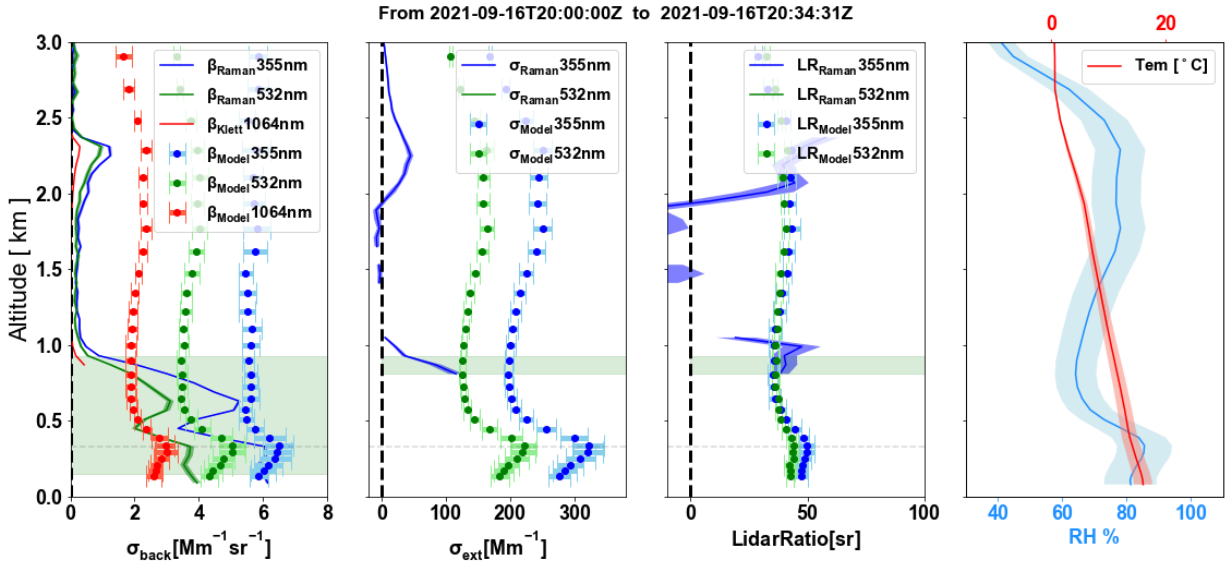

Figure S31: Profiles from 20:00 to 20:34 at UTC time on 2021-09-16.

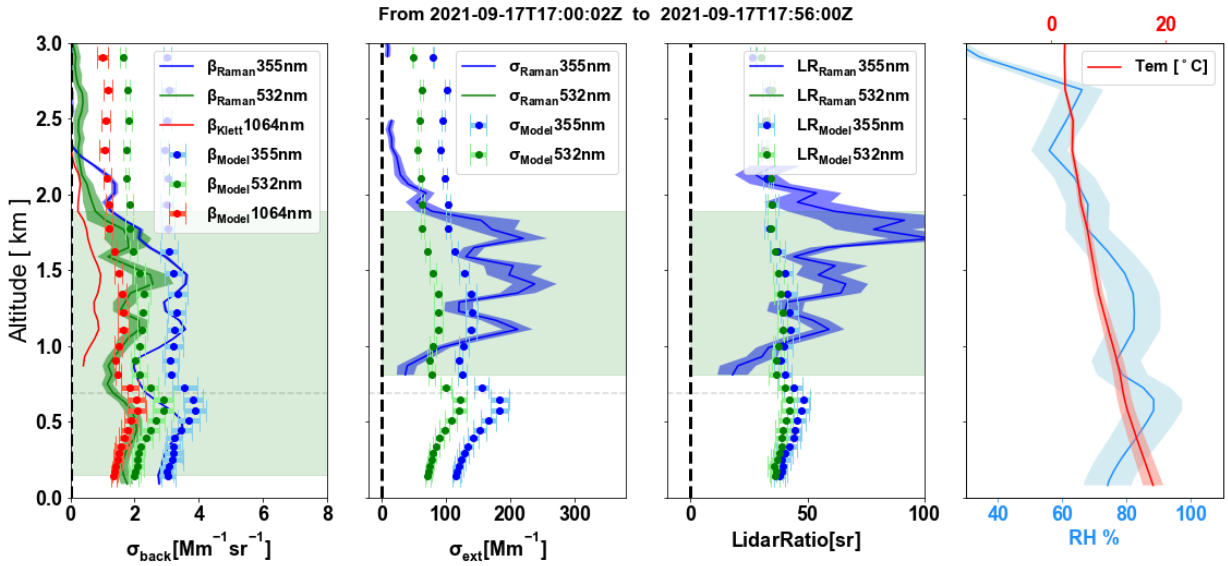

Figure S32: Profiles from 17:00 to 17:56 at UTC time on 2021-09-17.

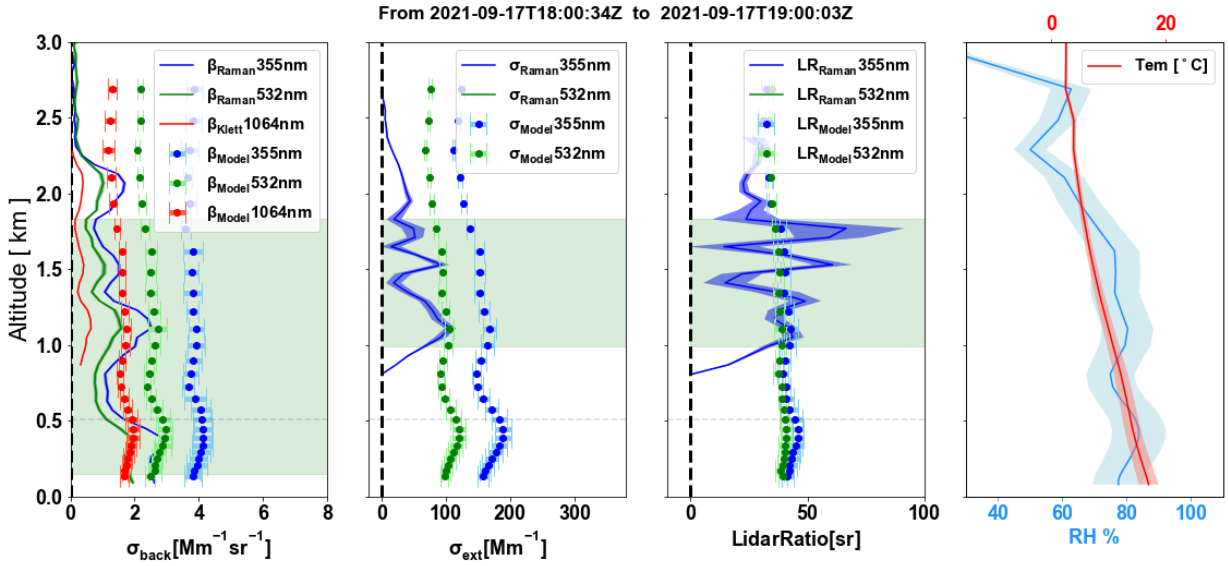

Figure S33: Profiles from 18:00 to 19:00 at UTC time on 2021-09-17.

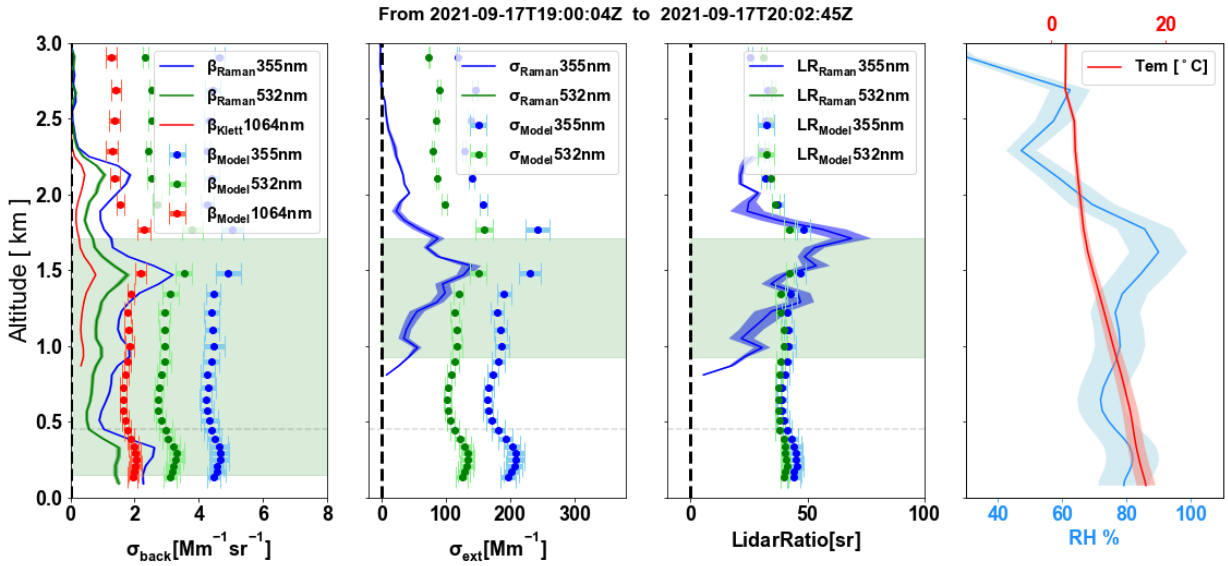

Figure S34: Profiles from 19:00 to 20:02 at UTC time on 2021-09-17.

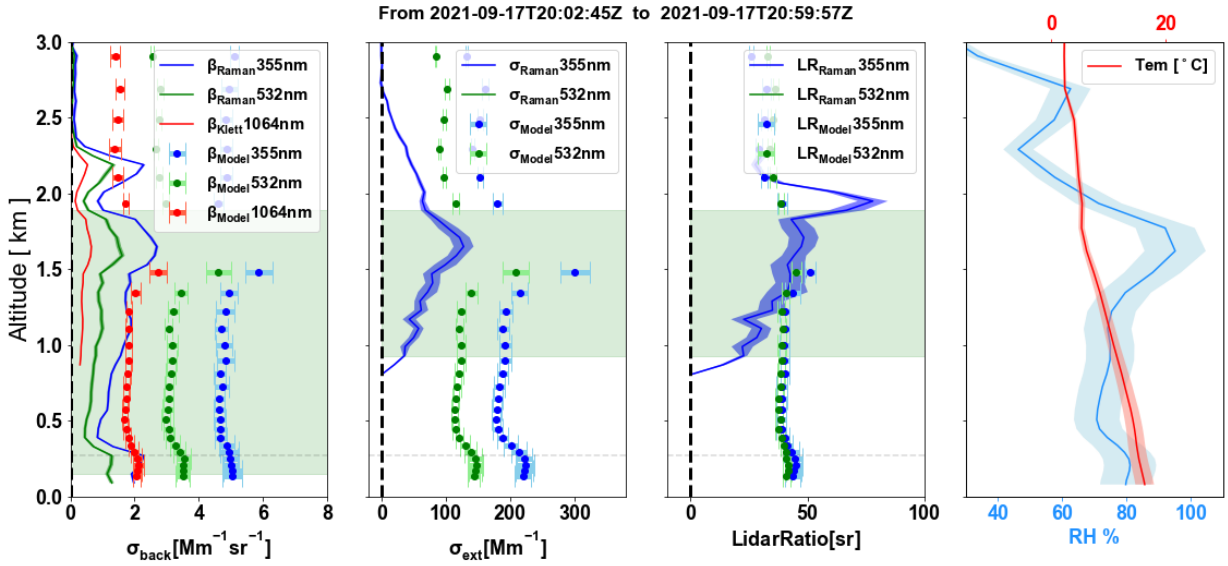

Figure S35: Profiles from 20:02 to 20:59 at UTC time on 2021-09-17.

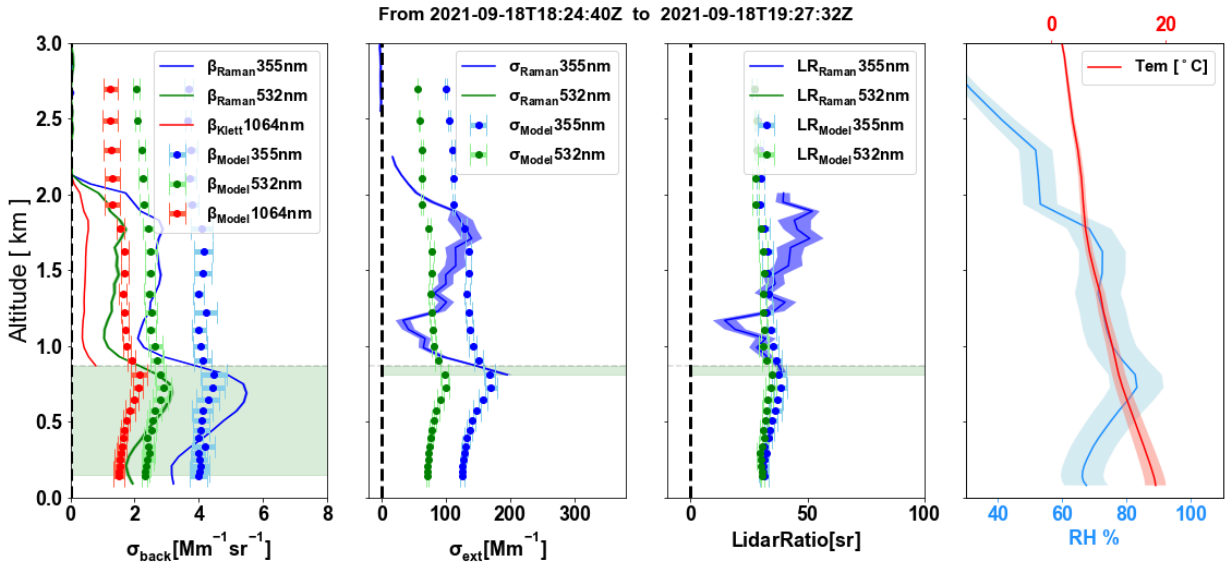

Figure S36: Profiles from 18:24 to 19:27 at UTC time on 2021-09-18.

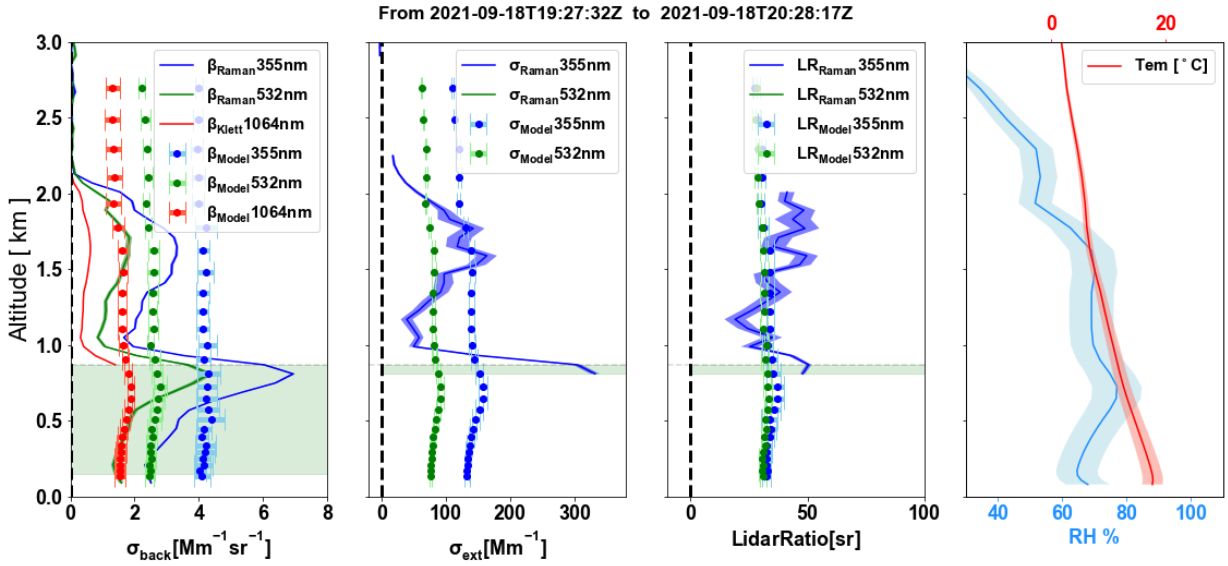

Figure S37: Profiles from 19:27 to 20:28 at UTC time on 2021-09-18.

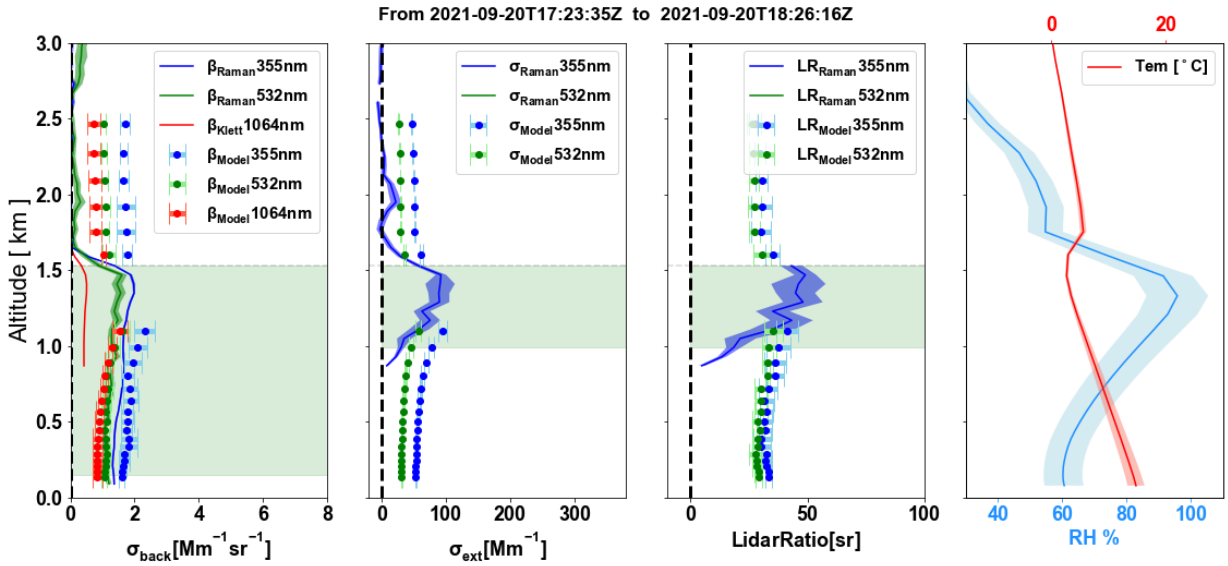

Figure S38: Profiles from 17:23 to 18:26 at UTC time on 2021-09-20.

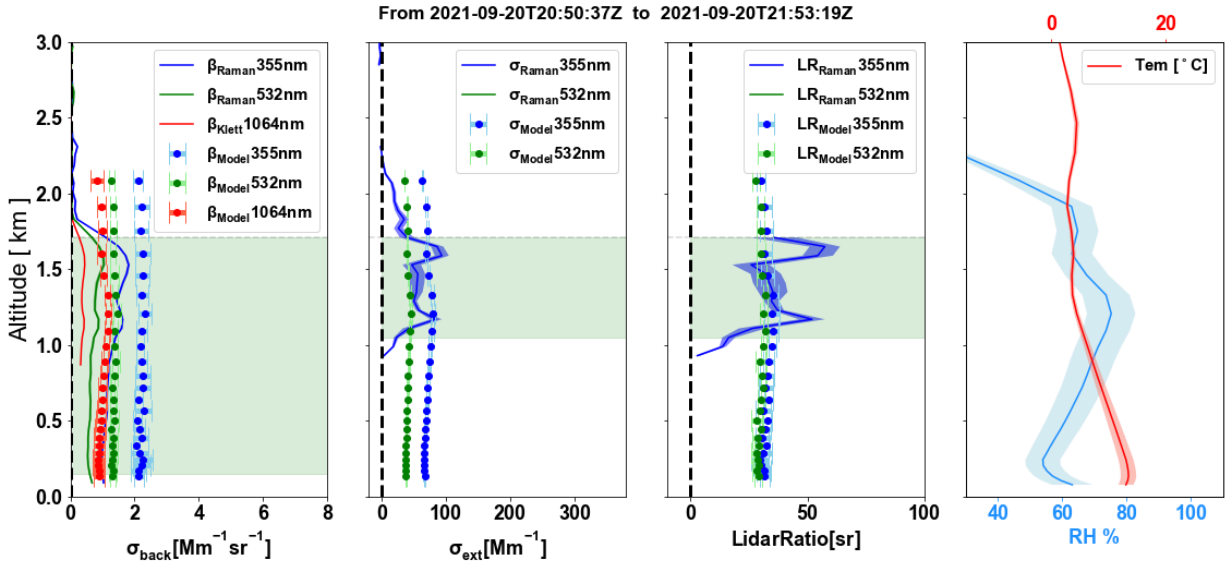

Figure S39: Profiles from 20:50 to 21:53 at UTC time on 2021-09-20.

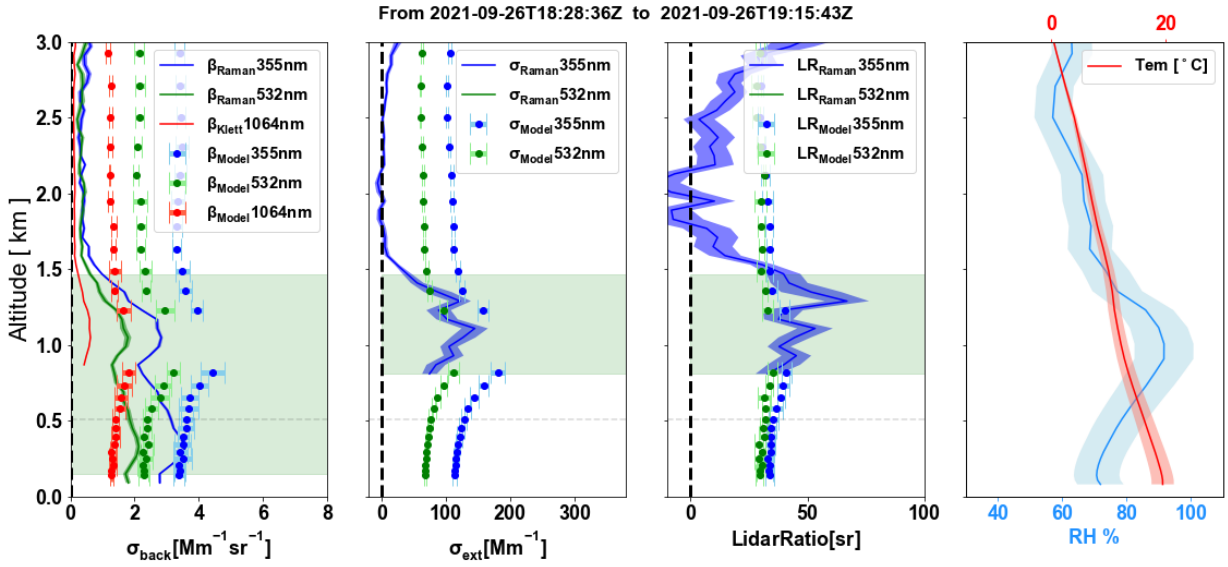

Figure S40: Profiles from 18:28 to 19:15 at UTC time on 2021-09-26.

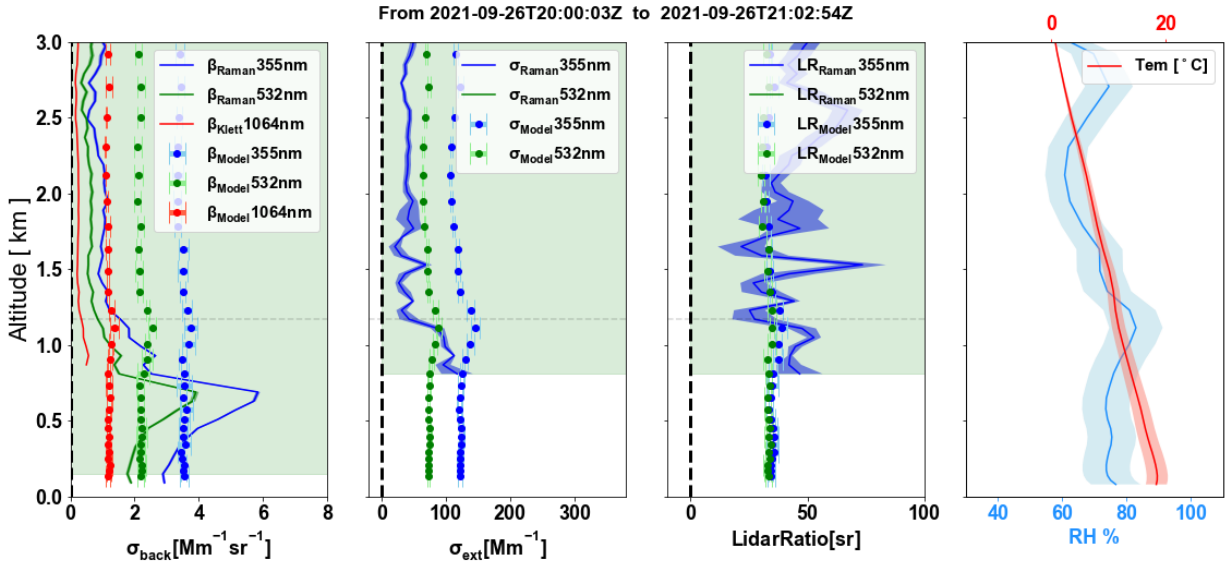

Figure S41: Profiles from 20:00 to 21:02 at UTC time on 2021-09-26.

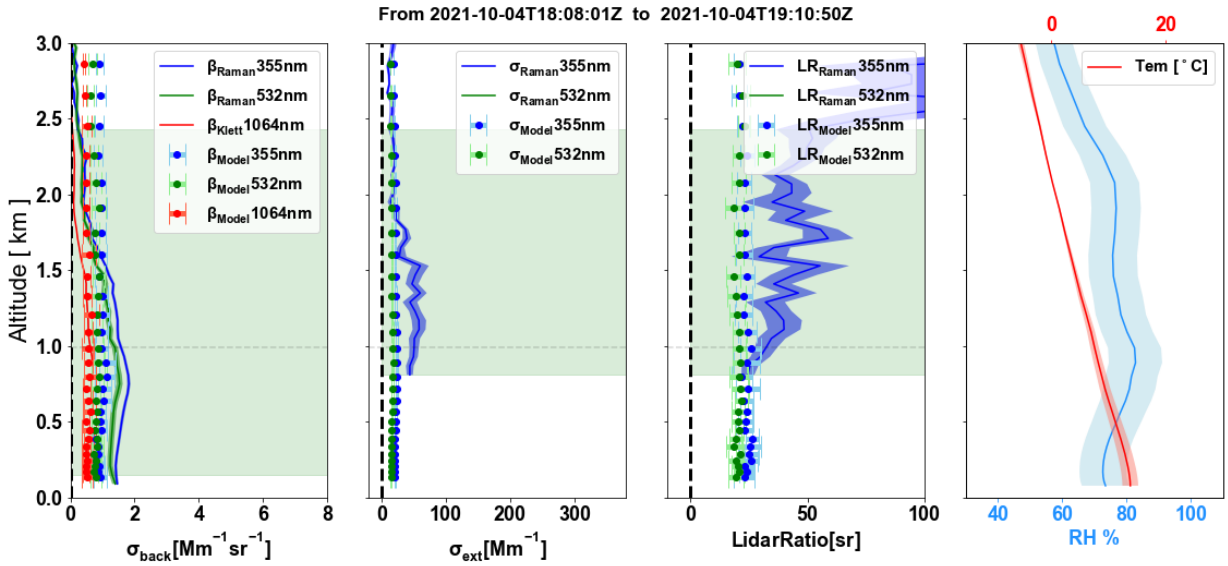

Figure S42: Profiles from 18:08 to 19:10 at UTC time on 2021-10-04.

S7 Tables:

Table S1 Model data availability at the Raman lidar measurements dates for all the instruments.

Lidar dates	ACSM	MAAP	SMPS	APS	Nephelometer	Meteorological	Model
2021-05-11							
2021-05-12							
2021-05-19							
2021-05-21							
2021-05-31	x	x	x	x	x		x
2021-06-01		x	x	x	x		x
2021-06-02		x	x	x	x		x
2021-06-07	x						x
2021-06-24							
2021-07-08							
2021-07-12							
2021-07-19							
2021-07-29							
2021-09-09							
2021-09-16				–			–
2021-09-17				–			–
2021-09-18				–			–
2021-09-20				–			–
2021-09-26				–			–
2021-10-04							

x:data not available; −: data available with assumptions of the coarse mode size distribution, see section S2.

Table S2 Lognormal fit parameters for the daily averaged APS volume size distribution from the Trolix-2019 campaign.

Date	Fit mu	Fit Sigma
9/14/2019	7.85	0.47
9/15/2019	7.84	0.51
9/16/2019	7.60	0.46
9/17/2019	7.73	0.48
9/18/2019	7.75	0.49
9/19/2019	7.81	0.47
9/20/2019	7.94	0.49
9/21/2019	8.11	0.62
9/22/2019	7.81	0.52
9/23/2019	7.69	0.46
9/24/2019	7.68	0.44
9/25/2019	7.58	0.43
9/26/2019	7.58	0.46
9/27/2019	7.56	0.41
9/28/2019	7.54	0.41
9/29/2019	7.57	0.41
9/30/2019	7.66	0.43
10/1/2019	7.56	0.40
10/2/2019	7.66	0.44
10/3/2019	7.66	0.45
10/4/2019	7.60	0.45
Mean	**7.70**	**0.46**
Std	**0.14**	**0.05**

Table S3 The Refractive index, density and kappa values of the chemical composition. The values follow [a] Zou et al.(2019), [b] Düsing et al. (2021), [c] Di Biagio et al. (2019), [d] Bi et al.(2018), Di Biagio et al.(2019), Zieger et al.(2017).

Chemical composition	RI (refractive index)	Density (g cm-3)	*k*
SIA	1.53 + 1e-6j	1.75	0.5-0.7
OA	1.47+0.02j[b]	1.40[a]	0.1[b]
EC	1.75+0.55j[b]	1.80[b]	0.0[b]
MD	1.56+0.006j[c]	2.65[e]	0.0[e]
SS	1.5+0.00j[d]	2.07[f]	1.1[f]
H_2O	1.333+0.00j[a]	1.00[a]	-

S8 the estimation of the Mineral Dust and Sea Salt

As the coarse mode chemical composition was not measured during the RITA campaign, we made use of the measurements obtained from the previous Trolix campaign in 2019.

Sea salt (SS) aerosols are prominently found in the atmosphere over the Netherlands. They originate from seawater, which is entrained into the atmosphere by breaking waves and spumes. Hence, the composition of pure sea salt aerosol reflects that of sea water, encompassing natural organic compounds and pollutants. In this research, sodium serves as the ideal tracer because it offers the advantage of minimal losses due to depletion, ensuring reliable measurements. The recovery rate for sodium prior to analysis using ICP-MS stands at 100%, guaranteeing dependable detections. Conversely, when considering chloride, atmospheric reactions may lead to interactions with sulfuric and nitric acids, potentially resulting in the depletion of Cl- ions within the aerosol. As such, the presence of SS was estimated based on:

SS = 3.26 * [Na+].

Where the factor 3.26 stems from the relative mass contribution of Na in North Sea water. This approach is adopted from Schaap et al(2010).

Mineral Dust (MD) is also part of the atmospheric aerosol mixture in the Netherlands(Denier van der Gon et al., 2010). Silicon (Si) and Aluminum (Al) have been identified as promising tracers for MD analysis, but both element analyses suffer from recovery issues. In our analyses, the Silicon was biased low (40% recovery) in the analysis because in the open destruction step with HF, SiF_4 is evaporated. In contrast, Al exhibited a considerably higher recovery rate, approximately 70%. Given the superior recovery rate of Al, we have opted to utilize Al elemental analyses as the basis for estimating atmospheric MD concentrations (Hendriks et al., 2008; Denier van der Gon et al., 2010). We correct the Al concentration for unrecovered material by division with 0.70. As SiO_2 and Al_2O_3 are the most abundant minerals for Si and Al, respectively, we represent the entire mixture as follows:

[Al-based mass] = [Al] * (1 + 1.5 * (M-O/M-Al)), where M-O = 16.0 and M-Al = 27.0

[Si-based mass] = [Si] * (1 + 2 * (M-O/M-Si)), where M-Si = 28.1

It's important to note that the MD mass estimated using Al and Si as tracers typically serves as a conservative estimate, representing a lower limit of the total MD mass. Then the volume concentration of the SS and MD can be obtained by dividing their mass concentrations by the corresponding densities, and those parameters are listed in Table S3.

References

Bi, L., Lin, W., Wang, Z., Tang, X., Zhang, X., and Yi, B.: Optical Modeling of Sea Salt Aerosols: The Effects of Nonsphericity and Inhomogeneity, J. Geophys. Res. Atmos., 123, 543–558, https://doi.org/10.1002/2017JD027869, 2018.

Di Biagio, C., Formenti, P., Balkanski, Y., Caponi, L., Cazaunau, M., Pangui, E., Journet, E., Nowak, S., Andreae, M. O., Kandler, K., Saeed, T., Piketh, S., Seibert, D., Williams, E., and Doussin, J. F.: Complex refractive indices and single-scattering albedo of global dust aerosols in the shortwave spectrum and relationship to size and iron content, Atmos. Chem. Phys., 19, 15503–15531, https://doi.org/10.5194/acp-19-15503-2019, 2019.

Denier van der Gon, H., Jozwicka, M., Hendriks, E., Gondwe, M., and Schaap, M.: Mineral Dust as a component of particulate matter, PBL Netherlands Environ. Assesment Agency, 160, 2010.

Düsing, S., Ansmann, A., Baars, H., Corbin, J. C., Denjean, C., Gysel-Beer, M., Müller, T., Poulain, L., Siebert, H., Spindler, G., Tuch, T., Wehner, B., and Wiedensohler, A.: Measurement report: Comparison of airborne, in situ measured, lidar-based, and modeled aerosol optical properties in the central European background -identifying sources of deviations, Atmos. Chem. Phys., 21, 16745–16773, https://doi.org/10.5194/acp-21-16745-2021, 2021.

Hendriks, E. C. J., Gon, H. A. C. D. Van Der, and Schaap, M.: Constraining the potential source strength of various soil dust sources contributing to atmospheric PM10 concentrations in Europe, 80015, 2008.

Schaap, M., Weijers, E. ., Mooibroek, D., Nguyen, L., and Hoogerbrugge, R.: Composition and origin of particulate matter in the Netherlands, RIVM Rapp., 69, 2010.

Zieger, P., Väisänen, O., Corbin, J. C., Partridge, D. G., Bastelberger, S., Mousavi-Fard, M., Rosati, B., Gysel, M., Krieger, U. K., Leck, C., Nenes, A., Riipinen, I., Virtanen, A., and Salter, M. E.: Revising the hygroscopicity of inorganic sea salt particles, Nat. Commun., 8, https://doi.org/10.1038/ncomms15883, 2017.

Zou, J., Yang, S., Hu, B., Liu, Z., Gao, W., Xu, H., Du, C., Wei, J., Ma, Y., Ji, D., and Wang, Y.: A closure study of aerosol optical properties as a function of RH using a K-AMS-BC-Mie model in Beijing, China, Atmos. Environ., 197, 1–13, https://doi.org/10.1016/j.atmosenv.2018.10.015, 2019.